Sustainable Energy & Fuels

ROYAL SOCIETY OF CHEMISTRY

PAPER

View Article Online
View Journal | View Issue

Cite this: *Sustainable Energy Fuels*, 2021, **5**, 1003

All-fiber acousto-electric energy harvester from magnesium salt-modulated PVDF nanofiber†

Biswajit Mahanty,‡[ab] Sujoy Kumar Ghosh, ‡§[a] Santanu Jana,[c] Krittish Roy,[a] Subrata Sarkar[a] and Dipankar Mandal *[d]

In this work, an all-fiber acoustoelectric nanogenerator (AAPNG) is fabricated by the hydrated metal salt ($MgCl_2 \cdot 6H_2O$) (Mg-salt) reinforced polyvinylidene fluoride (PVDF–Mg) nanofibers as an active layer and interlocked conducting micro-fiber-based electrode for converting mechanical and acoustic energies into useful electrical power. It has been found that the electroactive phase content (~84%) is enhanced in PVDF–Mg nanofibers due to the inter-molecular H-bonding moieties, the arrangement of the macromolecular chains of polyvinylidene fluoride (PVDF) in a layer-by-layer fashion, and the existence of an interfacial interaction between the Mg-salt and dimethylformamide (DMF) resonance structure and $-CF_2$ dipoles of PVDF. As a result, PVDF–Mg nanofibers possess superior piezoelectric charge coefficient ($d_{33} \approx 33.6$ pC N^{-1}) and figure of merit (FoM $\approx 12.7 \times 10^{-12}$ Pa^{-1}) with respect to neat PVDF nanofibers ($d_{33} \approx 22$ pC N^{-1} and FoM $\approx 9.7 \times 10^{-12}$ Pa^{-1}). Benefitting from the ultrafast response time of ~6 ms, AAPNG serves as an acoustoelectric sensor detecting low-frequency sound with an acoustic sensitivity (S_a) of 10 V Pa^{-1}, which is superior to that of neat PVDF nanofibers ($S_a \sim 266$ mV Pa^{-1}). With the overall acoustoelectric energy conversion efficiency of ~1.3%, AAPNG powers a range of commercial electronic gadgets, such as LEDs, capacitors, and LCDs. This makes it perfectly suitable for noise detection purposes as well as self-powered microphone applications. Additionally, AAPNGs can be realized as human motion monitoring systems, such as finger motion sensors that pave the way of futuristic robotic-based applications.

Received 9th August 2020
Accepted 27th December 2020

DOI: 10.1039/d0se01185a

rsc.li/sustainable-energy

1. Introduction

The requirement of energy is rapidly burgeoning worldwide, and the uses of low-powered electronic gadgets are also rapidly increasing.[1–3] The shrinkage in size and lower power consumption of electronic gadgets are of great interest for the future technology as well. In our modern life style, a constant power supply requirement is essential for twenty four hours a day. Conventional batteries have few limitations, including a limited lifetime, which require regular replacement or recharging. In addition, batteries contain toxic chemicals that are harmful to the environment and vulnerable to the human health; thus the removal of batteries is severely regulated. In this scenario, sustainable power sources with self-powered electronics are of great interest, and tremendous research has been carried out in the search of a green, renewable and non-exhaustible energy source. To establish these goals, piezoelectric and triboelectric nanogenerators that generate electricity from environmental mechanical vibration facilitate the realization of a self-powered energy harvesting system.[4–8] Among them, triboelectric nanogenerators have few limitations, including abrasion resistance, moisture sensitive and limited use in bio-signal detection, as two dissimilar materials need to effectively interact with each other. Hence, piezoelectric nanogenerators are a relatively appropriate candidate to convert mechanical energy into electrical energy in an ambient environment, which are useful in small-scale self-powered electronic devices and wireless sensors.[9–11] However, owing to brittleness and toxicity, inorganic piezoelectric nanogenerators are constrained in their energy harvesting applications. In contrast, organic piezoelectric materials, and in particular, poly(vinylidene fluoride) (PVDF) $-(CH_2-CF_2)_n-$ and its copolymers are one of the best alternatives as they show a high piezoelectric coefficient, excellent chemical stability, flexibility, lightweight property, and biocompatibility. In general, PVDF

[a]*Department of Physics, Jadavpur University, Kolkata 700032, India*

[b]*Department of Electronics and Communication Engineering, Saroj Mohan Institute of Technology, Guptipara, Hooghly 712512, India*

[c]*Department of Electronics, Netaji Nagar Day College, Kolkata 700092, India*

[d]*Institute of Nano Science and Technology, Knowledge City, Sector 81, Mohali 140306, India. E-mail: dmandal@inst.ac.in; dpkrmandal@gmail.com; Fax: +91-172-2211074; Tel: +91-172-2210075*

† Electronic supplementary information (ESI) available. See DOI: 10.1039/d0se01185a

‡ These authors contributed equally to this work.

§ Present address: School of Energy and Chemical Engineering, Ulsan National Institute of Science and Technology (UNIST), Ulsan Metropolitan City 44919, Republic of Korea.

shows four distinct crystalline polymorphs, such as α-, β-, γ- and δ-phases.[12] Among them, β-, γ- and δ-phases are mainly polar crystalline phases that exhibit piezoelectricity in PVDF. Thus far, it has been shown that β-phase possesses the highest piezoelectric response. The macroscopic polarization of PVDF depends on the orientation of the molecular $-CH_2/-CF_2$ dipoles in the β-phase and degree of crystallinity. The electrical poling and mechanical stretching are the key factors to induce the formation of electroactive phases in PVDF.[14] However, these are very much cumbersome, cost- and time-intensive methods, and the PVDF films often lose their mechanical flexibility and durability. Also, electrical poling needs a very high electric field ($\sim$100 kV mm^{-1}). All of these limitations can be overcome by implementing the electrospinning process, where the β-phase can be directly nucleated by a combination of *in situ* electric poling and mechanical stretching.[13] In particular, compared to 1D materials synthesized by other methods, the nanofibers prepared by electrospinning have larger specific surface areas, higher aspect ratio, low cost, high reproducibility and better pore interconnectivity, which are favourable for energy conversion and storage.[15] Although there are several reports on the PVDF nanofibers-based energy harvesting device, the acoustic-pressure and human-motion dual driven all-fiber based textile sensor was rarely reported. The conventional approach towards the design of piezoelectric nanogenerators is the use of metal foil electrodes or metal-coated thin film electrodes as the charge collector, which limits the device life time under an extended cyclic stress.[16] There are a few more limitations, which includes the poor fatigue resistance causing early failure of the metal foils, as well as the huge mismatch of the Young's modulus and Poisson's ratio of the metal coating electrode and the polymer-based active material. As a result, during prolonged use, a loss of mechanical integrity and electric connectivity is often noticed. These limitations of the existing devices can be avoided by exploring a durable and efficient all-fiber nanogenerator, where both active component and electrodes are composed of flexible and soft fiber arrays. Furthermore, the performances of PVDF nanofibers are improved remarkably by the addition of some external-fillers.[13,17,18] In this context, a hydrated Mg-salt was incorporated as a filler in this work, which enhanced the yield of the β-phase in PVDF. It is important to mention that the small kinetic energy power generator developed so far is based on the conversion of mechanical forces. The origin of mechanical energy can be acquired from wind, water flow, air flow, machinery, tides and different transport systems. It is found that most of the published works are based on the motion of the bodies as mechanical energy harvesters. On the other side, large amounts of acoustic/sound energy from humans talking, vehicles, electronic instruments, music, construction sites, power plants and many others are one of the clean, sustainable energy and ubiquitous resources. In general, the conversion of sound energy to electricity, referred to as "acoustoelectric conversion", is used to exhibit acoustic sensors, music instruments and microphone applications due to the small electric output generated. As the microphone has the capability of converting the sound energy into an electrical signal, hence our proposed device AAPNG could be used as a self-powered microphone for future human–machine interactions. However, in this framework, acoustoelectric devices and mechanical energy harvesters are both developed based on piezoelectricity.

In this work, a remarkable improvement of the electroactive phase content in an electrospun PVDF nanofiber has been gained by synergistic effect of the interfacial interactions of Mg-salts with a PVDF chain, and the additional mechanical stretching during the collection of the fiber by a high-speed rotating collector. Additionally, a highly sensitive all-fiber acousto- and piezo-electric nanogenerator has been designed with PVDF–Mg salt based nanofibers, which are able to detect the low-frequency sound with a maximum available acoustic sensitivity (S_a) of $\sim$10 V Pa^{-1} with the overall acoustoelectric energy conversion efficiency of 1.3%. Finally, it can be used as a finger sensor, which generates different output responses to detect different types of finger bent oscillation. In addition, the practical applicability of AAPNG as a self-powered piezoelectric energy harvester is demonstrated by the successful charging of the capacitor. Thus, AAPNG is promising for use as a pressure sensor, self-powered microphone, mechanical and acousto-electric energy harvester, and also as an effective power source for portable personal electronic gadgets.

2. Results and discussion

Structural and electrical properties

The field-emission scanning electron microscopy (FE-SEM) image with the corresponding histogram profile of the PVDF–Mg nanofibers is presented in Fig. 1a. It was observed that the nanofibers were successfully fabricated without any bead defects. It should be noted that the average diameter of the PVDF–Mg electrospun nanofiber ($\sim$130 nm) decreases in comparison to neat PVDF nanofibers ($\sim$180 nm) due to the addition of the Mg-salt in PVDF solution (see Fig. S1, ESI†). This is attributed to the viscoelasticity, surface tension of the solution, and charge density carried by the solution jet that is affected by Mg-salt into the PVDF solutions.[19]

The Mg-salt incorporated PVDF-DMF solution was stirred for 2 days. Due to its hydrophilic and polar aprotic nature, the atmospheric moisture was slowly absorbed concurrently. As a result, the water molecules from the moisture enclosed the F^- ions of the PVDF in cooperation with the coordination water of the Mg-salt ($MgCl_2 \cdot 6H_2O$). Therefore, due to the strong H-bonding interaction of the water molecules on the part of the F^- of PVDF (*i.e.*, O–H$\cdots$F–C), the $-CH_2/-CF_2$ dipoles get oriented unidirectionally in PVDF (Fig. 1b).[20] In the Mg-salt incorporated PVDF-DMF solution, a resonance structure between DMF and Mg^{2+} exists, which is observed in the FT-IR spectra (Fig. 1c).[21] This is in accordance with the coordinate site, DMF, having two feasible ligands, *i.e.*, the C=O and C–N bonds for oxygen and nitrogen, respectively. To measure the strength of the mutual actions between the metal and non-aqueous solvent molecules, Gutmann has initiated the donor number (DN) and acceptor number (AN) for the measurement of the nature of the solvent, such as basic and acidic, respectively.[21] Thus, DMF behaves as a strong donor because it possesses the values of DN $\sim$ 27.8 and

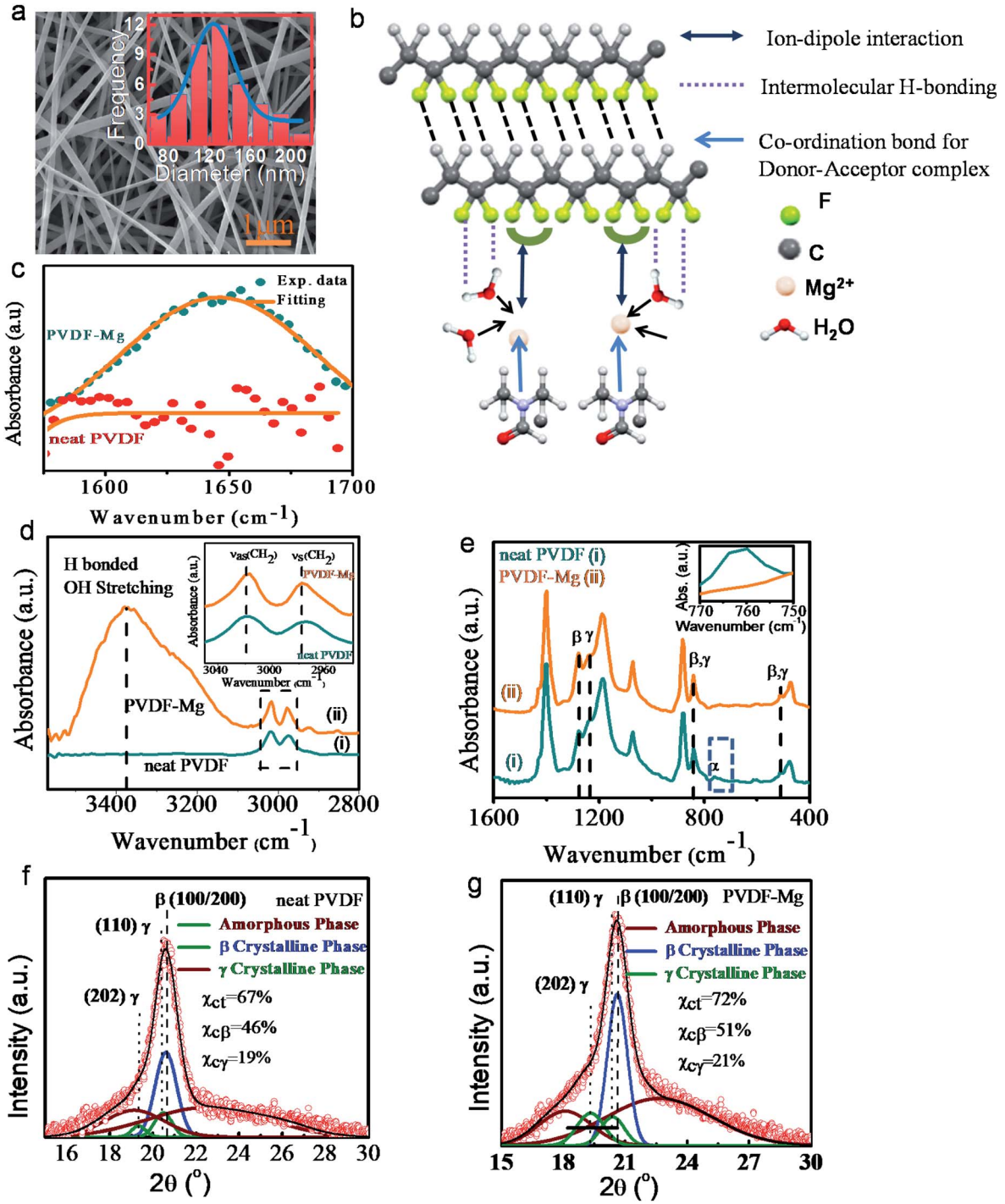

Fig. 1 (a) FE-SEM images of the electrospun nanofiber mat of the PVDF–Mg nanofiber with a histogram plot of the nanofiber diameter distribution placed in the inset. (b) Schematic representation of the β-phase nucleation process in the PVDF–Mg nanofibers. (c) The FT-IR spectra of the neat PVDF and PVDF–Mg nanofiber in the wavenumber region of 1575–1700 cm^{-1}. (d) FT-IR spectra of the neat PVDF and PVDF–Mg fibers mat in the wavenumber region from 3700 to 2800 cm^{-1} and (e) 1600 to 400 cm^{-1}. A separate enlarged view (3100 to 2900 cm^{-1}) for the demonstration of the frequency shifting of the CH_2 stretching vibration is shown in the inset of Fig. 1d. The XRD patterns and their curve deconvolution of the (f) neat PVDF and (g) PVDF–Mg fibers mat. The degree of crystallinity of the β and γ-phases is also provided.

AN ~ 13.6, which are very close to pyridine (DN ~ 33.1, AN ~ 14.2). The appearance of the stretching vibrational band ($\nu_{C=O}$) at 1645 cm^{-1} (not present in the neat PVDF nanofibers) implies that DMF forms a resonance structure with the Mg-salt (Fig. 1c). The frequency range starts from 3700 to 2800 cm^{-1}, and a wide absorption band exists that represents the presence of the H-bonding interaction (Fig. 1d).[20,22] This widening of the absorption band exists because of the change of the micro-

environments in the ground state of the –OH stretching vibration. As depicted in Fig. 1b, due to the intermolecular H-bonding, the PVDF moieties are arranged in a layer-by-layer fashion.[22] Furthermore, an interfacial interaction exists between the Mg-DMF resonance structure and $-CF_2$ dipoles. As a result, there is a clear stretching of the $-CH_2$ dipoles that is present. It is also important to mention that there is a clear shifting of the CH_2 asymmetric (ν_{as}) and symmetric (ν_s) stretching vibrational bands, which are present toward the lower frequency region with respect to the neat PVDF nanofibers, as shown in the inset of Fig. 1d (marked with the square box).[13]

The effective mass of the $-CH_2$ dipoles was improved due to the interfacial interactions. Therefore, due to damping, a reduction in the vibrational frequency (*i.e.*, wavenumber) of the asymmetric and symmetric CH_2 stretching vibration is visible. The damping constant ($2r_{dc}$) is related to the wavenumber ($\bar{\lambda}_{int}$) of the CH_2 stretching vibration (ν-CH_2) as:

$$\bar{\lambda}_{int} = \left[\bar{\lambda}_0^{\,2} - \left(\frac{r_{dc}}{2\pi c}\right)^2\right]^{\frac{1}{2}} \quad (1)$$

where $\bar{\lambda}_0$ is the wavenumber of (ν-CH_2) in the damping-free vibration present in the neat PVDF film, $\bar{\lambda}_{int}$ is the corresponding wavenumber due to the damped vibration in the PVDF–Mg nanofibers, and c is the velocity of light. The estimated damping constant ($2r_{dc}$) using eqn (1) is 42.3×10^{11} s^{-1} with respect to the neat PVDF. So, it is finally concluded that the enhancement of the damping constant ($2r_{dc}$) happened due to the improvement of the interfacial interaction, and it enhances the β-phase content as well.

The FT-IR spectra of the neat PVDF, as well as PVDF–Mg nanofibers, are presented in Fig. 1e. The respective vibrational bands are labeled according to the presence of the crystalline phases in the region of 1600–400 cm^{-1}. The neat PVDF nanofibers contain a hetero-phase structure, *i.e.*, nonpolar α-phase (at 762 cm^{-1} in the inset of Fig. 1e) and polar β-, γ-phases (at 1275 and 1236 cm^{-1}, respectively).[13] However, the PVDF–Mg nanofibers contain a homo-phase structure, *i.e.*, only polar β- and γ-phases and no peak for the α-phase were available in the spectrum. It is obvious that the full conversion of the polar phases (β-, γ-phases) in the PVDF–Mg nanofibers has occurred with respect to the neat PVDF nanofibers by electrospinning technique. It should be noted that both nanofibers contain the 841 cm^{-1} vibrational band, which indicates the presence of the β- and γ-phases, simultaneously. On the other hand, the vibrational band at 510 cm^{-1} also indicates the signature of both β- and γ-phases (polar) simultaneously in the PVDF–Mg nanofibers. The electroactive phase content was calculated using the Beer–Lambert law,

$$F_{EA} = \frac{A_{841}}{\left(\frac{K_{841}}{K_{762}}\right)A_{762} + A_{841}} \times 100\%, \quad (2)$$

where A_{762} and A_{841} represent the absorbances at 762 and 841 cm^{-1}, respectively, $K_{762} = 6.1 \times 10^4$ cm^2 mol^{-1} and $K_{841} = 7.7 \times 10^4$ cm^2 mol^{-1}, representing the absorbance coefficient corresponding to the wavenumbers.[14,17] Therefore, the calculated F_{EA} of the neat PVDF nanofibers is $F_{EA} \sim 74\%$, whereas in the case of the PVDF–Mg nanofibers, $F_{EA} \sim 84\%$.

The crystallinity of the neat PVDF and PVDF–Mg nanofibers were estimated from the XRD pattern using the curve deconvolution process, demonstrated in Fig. 1f and g. As shown in Fig. 1f and g, the induced electroactive β- and γ-phases have been estimated from the curve-deconvoluted XRD pattern.[22,23] In the electrospun nanofibers, the α-characteristic diffractions (17.6°, 18.2° and 19.7°) are reduced. On the other hand, the peaks from the electroactive β- and γ-phases (18.7°: $\gamma_{(202)}$, 20.3°: $\gamma_{(110)}$ and 20.8°: $\beta_{(110/200)}$) appeared (shown in Fig. 1f and g).[12,25] The curve-deconvoluted diffraction peaks at 18.7° (202) and 20.3° (110) are attributed to the existence of a smaller amount of γ-phase with the co-presence of the major β-phase content, as affirmed from its acute diffraction peak at 20.8° (110/200).[24,25] As the Mg-salt was combined, the diffraction peak area of the β crystals (20.8°) was improved. Thus, the Mg-salt added electrospun fibers consist of mostly β-phase with a very low quantity of the γ-phase. Applying the deconvolution method, the amount of overall crystallinity and the existence of the β- and γ-phases were separately estimated. The overall degree of crystallinity (χ_{ct}) is calculated from

$$\chi_{ct} = \frac{\sum A_{cr}}{\sum A_{cr} + \sum A_{amr}} \times 100\% \quad (3)$$

where $\sum A_{cr}$ and $\sum A_{amr}$ are the total integral area due to the crystalline peaks and amorphous halo, respectively.[12,22,24] It was found that the overall crystallinity in the PVDF–Mg electrospun nanofibers was ~72%, which is superior to the neat PVDF nanofibers (*i.e.*, $\chi_{ct} = 67\%$). The β- and γ-phase content can be evaluated from the following eqn (4) and (5):

$$\chi_{c\beta} = \chi_{ct} \times \frac{\sum A_\beta}{\sum A_\beta + \sum A_\gamma}\% \quad (4)$$

and

$$\chi_{c\gamma} = \chi_{ct} \times \frac{\sum A_\gamma}{\sum A_\beta + \sum A_\gamma}\% \quad (5)$$

where $\sum A_\beta$ and $\sum A_\gamma$ indicate the total integral area from the β and γ-crystalline phase peaks, respectively. The β- and γ-phase content ($\chi_{c\beta} \sim 51\%$ and $\chi_{c\gamma} \sim 21\%$) in the PVDF–Mg nanofibers are improved in comparison to that of neat PVDF ($\chi_{c\beta} \sim 46\%$ and $\chi_{c\gamma} \sim 19\%$), as indicated in Fig. 1e and f. As a result, the addition of a little amount of Mg salt significantly affects the consequent crystalline properties of PVDF.[26,27] This increment of crystallinity of the PVDF is ascribed as the (i) reduced structural defects in the PVDF–Mg nanofibers by the nano-confinement effect,[28,29] (ii) imposing restriction in the molecular arrangement of PVDF, which is known as the "molecule movement restriction" effect,[30] and (iii) as heterogeneous nucleating agents, the Mg-salt promotes the transformation of local amorphous regions into ferroelectric crystalline phases.[31]

The crystallite sizes of the β (*i.e.*, D_β) and γ (*i.e.*, D_γ) phases were evaluated from the Debye–Scherrer equation, as mentioned below:

$$D = \frac{K\lambda}{\beta \cos \theta} \quad (6)$$

where K is the constant (0.89) value, λ is the wavelength (0.1541 nm) of the Cu-K_α X-ray radiation, β is the full-width (in radian) at half maximum (FWHM) of the intense diffraction peak, and θ is the diffraction angle. The estimated values of the crystallite size of the β- (*i.e.*, $D_\beta \sim 7$ nm) and γ- (*i.e.*, $D_\gamma \sim 6$ nm) phases of the PVDF–Mg nanofibers are smaller than those of the neat PVDF nanofibers ($D_\beta \sim 9$ and $D_\gamma \sim 8$ nm). It is worth mentioning that the decrement of the crystallite size helps the molecular $-CH_2/-CF_2$ dipoles to be more active for the piezoelectric properties.[32] It is clearly observed that the χ_{ct} and β-phase are relatively increased when the Mg-salt is added. In addition, it was found to be superior to that of the neat PVDF nanofibers. Thus, the Mg-salt added PVDF nanofibers will display the improved piezoelectric response, as it is directly proportional to the β-crystallinity and the degree of dipole orientations.[33]

Piezoelectric energy harvesting

To demonstrate the application of the materials, we have fabricated a PVDF–Mg based all-fiber nanogenerator/energy harvester. The piezoelectric energy harvesting performance is depicted in Fig. 2. The AAPNG generates an open circuit output voltage of 8.5 V using a repetitive finger imparting under vertical stress amplitude of $\sigma_a \approx 15$ kPa on the surface of the nanogenerator from 6 cm height. It has been observed that the generated open circuited output voltage is superior to the neat PVDF-based nanogenerators (Fig. 2a) under the same conditions. Furthermore, the energy harvesting performance of AAPNG is demonstrated by repeating finger imparting under different pressure amplitude (σ_a) from 5.25–18.25 kPa, as

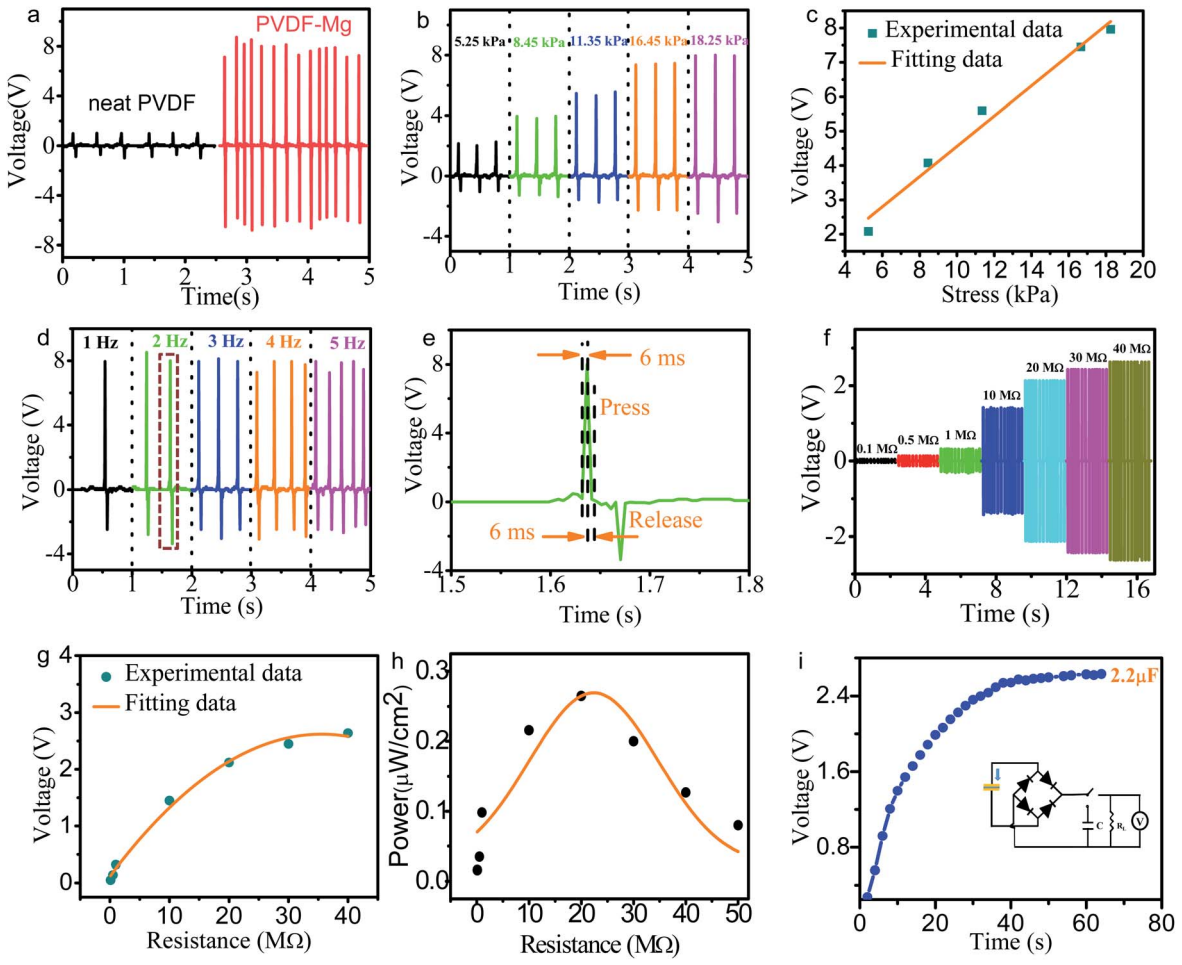

Fig. 2 Energy harvesting characterizations of the nanogenerators. (a) Measured bidirectional open circuit output voltage of the piezoelectric electrospun energy harvester (AAPNG) and neat PVDF based nanogenerator under repeated finger imparting when the pressure amplitude is 14.85 kPa. (b) Pressure-dependent output open-circuit voltage (V_{oc}) of A-PNG. (c) Study of the output open-circuit voltage (V_{oc}) with applied pressure (σ_a). (d) Performance characterisation of A-PNG under different frequency conditions. (e) The expanded view of the output positive voltage (press) and negative voltage (release) pulse signal of the marked cycle in (d). (f) The variation of the output voltage with external load resistances. (g) Study of the nature of the output voltage change with different load resistor. (h) Instantaneous power output as a function of the external load resistance, indicating the maximum power output is obtained at 23 MΩ. (i) Capacitor-charging performance of the A-PNG. Schematic of the charging and output voltage measurement circuit as a function of the external load is given in the lower right inset.

illustrated in Fig. 2b. It is obvious that the output open-circuit voltages of AAPNG was enhanced increasingly with input pressure amplitude (σ_a), and it is important to mention that a marginal increase of the output voltage is achieved after 16.45 kPa of the applied imparting pressure amplitude. This is due to the fact that the displacement of the ionic charge within a crystal deformation greatly depends on the applied mechanical pressure.[34] It is assumed that the applied pressure amplitude of 16.45 kPa is enough to reach the boundary value of the ionic displacement of the crystal deformation for the PVDF–Mg salt based energy harvester. Therefore, no remarkable change in the output-generated voltage was observed when the applied pressure amplitude (σ_a) exceeded ~16.45 kPa under the repetitive finger imparting condition. The developed output voltage varies almost linearly corresponding to the increased applied stress amplitude in the smaller pressure regime, which is consistent with the piezoelectric theory, as seen in Fig. 2c. The average mechano-sensitivity (S_M), defined as $S_M = (\Delta V_{oc}/\Delta\sigma_a)$, has been estimated to quantify the dynamic mechanical stimuli sensing ability, where ΔV_{oc} and $\Delta\sigma_a$ are the changes of the output voltage and pressure, respectively.[17] It was found to be ~0.44 V kPa^{-1} from the slope of the curve of Fig. 2c in the pressure range of 5.25–18.25 kPa, which is superior to the previously reported piezoelectric nanogenerators (see Table S1, ESI†) due to the striking role of the Mg-salt incorporation PVDF nanofibers. Hence, the AAPNG is a suitable candidate in biomedical applications, such as vocal cord response during laughing and coughing action, speech signal recognition, and swallowing response as a self-powered pressure sensor. The performance of the AAPNG was characterised by changing frequency of the applied stress in the range of 1 to 5 Hz upon the surface of the nanogenerator under a constant imparting stress amplitude of 18 kPa (Fig. 2d). Importantly, the expanded view of the positive pulse (press) and negative pulse (release) signal of the rectangular dotted marked cycle in Fig. 2d is depicted in Fig. 2e. It was observed that AAPNG showed the ultrafast response time and reset time of ~6 ms, which is much better than that of the few reported piezoelectric based nanogenerators.[35] As a result, AAPNG has the capability to be used in ultrafast signal detection in sensory applications. The performance of AAPNG can also be affected by the external resistance. The different values of the load resistors (R_L) are applied for measuring the output voltage, and clearly shows that the performance of the device is affected by the load resistors (shown in Fig. 2f) under a constant pressure condition ($\sigma_a \sim 7$ kPa). As the load resistance increased, the generated voltage becomes larger and is saturated at infinitely high resistance (R_L) (~40 MΩ), corresponding to the open circuit voltage, as evident from Fig. 2g. Interestingly, the instantaneous power density (P) of the AAPNG is estimated taking in account the eqn.

$$P = \frac{V^2}{A \cdot R_L}, \tag{7}$$

where A is the effective surface area of the device, and V_L is the load voltage across the load resistance R_L. The variation of the output power density (P) with the external load resistor (R_L) is shown in Fig. 2h. It is seen that the instantaneous power density (P) increases in nature with the load resistance (R_L), and reached the maximum value of 0.28 μW cm^{-2} at R_L of 23 MΩ, operating under a repeated finger imparting pressure amplitude of ~7 kPa. Beyond 23 MΩ, the instantaneous power density (P) is in decreasing nature. As per circuit theory, the maximum power is delivered to the load resistor from the source, as impedance matching exists between the internal and external systems; hence, $R_L \approx R_i \approx 23$ MΩ (internal resistance of the device). Therefore, it is now concluded that AAPNG could operate effectively when the load resistance is in the order of ~23 MΩ. This continuous power output is capable of simultaneously and instantly powering commercial LEDs to glow. In the interest of demonstrating a practical application of AAPNG, the device was attached to the external capacitor ($C = 2.2$ μF) through a full-wave bridge rectifier circuit, as shown in the inset of Fig. 2i. The capacitor ($C = 2.2$ μF) was charged up to a saturated voltage of ~2.6 V at 65 s exponentially under a constant finger imparting pressure amplitude of 7 kPa (as shown in Fig. 2i). The charging time constant (τ) was defined as the time required recovering to $(1 - 1/e)$ or (63%) of the steady state voltage by the capacitor, and is estimated as τ ~14 s. It is obvious that the charging behaviour of AAPNG is superior to all fibers nanogenerators (see Table S2, ESI†). The power (P) and stored energy (W) are being estimated by the following eqn (8) and (9), respectively,

$$P = \frac{CV_s^2}{2t} \tag{8}$$

and

$$W = \frac{CV_s^2}{2}, \tag{9}$$

where C is the capacitance of the capacitor, V_S is the saturation voltage, and t is the time required to reach the saturation voltage. However, the calculated maximum power (P) and energy (W) stored in the capacitor ($C = 2.2$ μF) are 0.12 μW and 7.61 μJ, respectively. The superior energy scavenging performance of AAPNG is associated with the larger piezoelectric charge coefficient ($d_{33} = g_{33} \times \varepsilon_0 \times \varepsilon_r \approx 33.6$ pC N^{-1}) than the neat PVDF ($d_{33} \approx 22$ pC N^{-1}),[13] where g_{33} is the piezoelectric voltage coefficient, ε_0 is the permittivity of the free space (~8.85 × 10^{-12} F m^{-1}) and $\varepsilon_r \approx 10$ at 1 kHz is the dielectric constant of the PVDF–Mg composite nanofibers.[24] The d_{33} value of the PVDF–Mg nanofibers is remarkably greater in comparison to the various PVDF-based nanofibers. A comparison of the nanofibers is shown in Table S3, ESI.† Now, the voltage coefficient, $g_{33} \sim \frac{V_{oc}}{\sigma_a \times t} = 0.38$ V m N^{-1}, where $\sigma_a = 15$ kPa is the stress magnitude and t is the thickness of AAPNG. Thus, it displays a superior piezoelectric figure of merit[36,37] (FoM ≈ $d_{33} \times g_{33} \approx 12.7 \times 10^{-12}$ Pa^{-1}) with respect to neat PVDF (FoM ≈ 7 × 10^{-12} Pa^{-1}). Furthermore, it has been observed that the nanogenerator shows lower output voltage upon repeated bending and releasing motion (ESI, Fig. S2†), in comparison to vertical stress. When the device was subjected to vertical stress (along 33 directions), the d_{33} parameter of the device was

responsible for the energy generation. On the other hand, upon bending releasing motion (along 31 directions), the d_{31} parameter of the device was responsible for the energy generation. In this case, d_{33} was higher than d_{31}, meaning that the dipoles are oriented along the thickness direction and the air-permeable nanofibers are more mechanically responsive along the thickness (z) direction.

Befitting from such extraordinary performances, AAPNG was demonstrated as an acoustoelectric device that effectively converted acoustic energy into an electric signal to generate power. To do this, AAPNG was simply attached to a sound speaker. The AAPNG produces the periodic open-circuit output voltages with peak values of ~2 V and ~3 V under a sound pressure level (SPL) of 80 and 120 dB, and frequency of 130 Hz, respectively (see Fig. 3a and b). Here, it is worth mentioning that the generated output voltage depends on SPL with constant sound frequency. The fast Fourier transform (FFT) corresponding to the voltage waveforms in Fig. 3a and b is presented in Fig. 3c and from the processed output profile, it was found that the corresponding resonance frequency of the device was shifted towards 126 Hz, while it was in coherence with the input sound frequency at 80 dB. As a result, AAPNG could be applicable in noise pollution monitoring, as well as in self-powered microphone application. On the other hand, AAPNG could convert the environmental noise (such as traffic, construction sites, public places) to generate an electric signal. The acoustic sensitivity (S_a) can be evaluated from the eqn (10),

$$S_a = \frac{V}{p_a} = \frac{V}{P_0 10^{L_p/20}} \quad (10)$$

where V is the output voltage, p_a is the employed sound pressure, P_0 is the reference pressure of 0 dB (~0.00002 Pa) and L_p is the SPL in dB of the employed sound vibration (80 dB).[17] Hence, the estimated maximum available acoustic sensitivity ($S_a \sim 10$ V Pa^{-1}) is superior to that of the neat PVDF nanofibers-based sensor ($S_a \sim 266$ mV Pa^{-1}).[38] Therefore, it may be concluded that AAPNG can be operated as an excellent sound or acoustic sensor.

The instantaneous acousto-electric energy conversion efficiency (η_{acoust}) of AAPNG is defined as the ratio of the electric power output (P_e) to the acoustic power input

$$(P_a)\colon \eta_{acoust} = \frac{P_e}{P_a}. \quad (11)$$

The optimum resistance ($R_i \approx 23$ MΩ) was connected with AAPNG to derive the optimized output performance, and the output voltage per cycle was measured instantaneously, as shown in Fig. 3b, d and e.

$$P_e = \int_0^t \frac{V(t)^2}{R} dt \times f_a, \quad (12)$$

where f_a is the sound wave frequency.[38] The estimated output energy is $P_e = 8.36 \times 10^{-6}$ W.

The input acoustic power was calculated using the eqn (13):

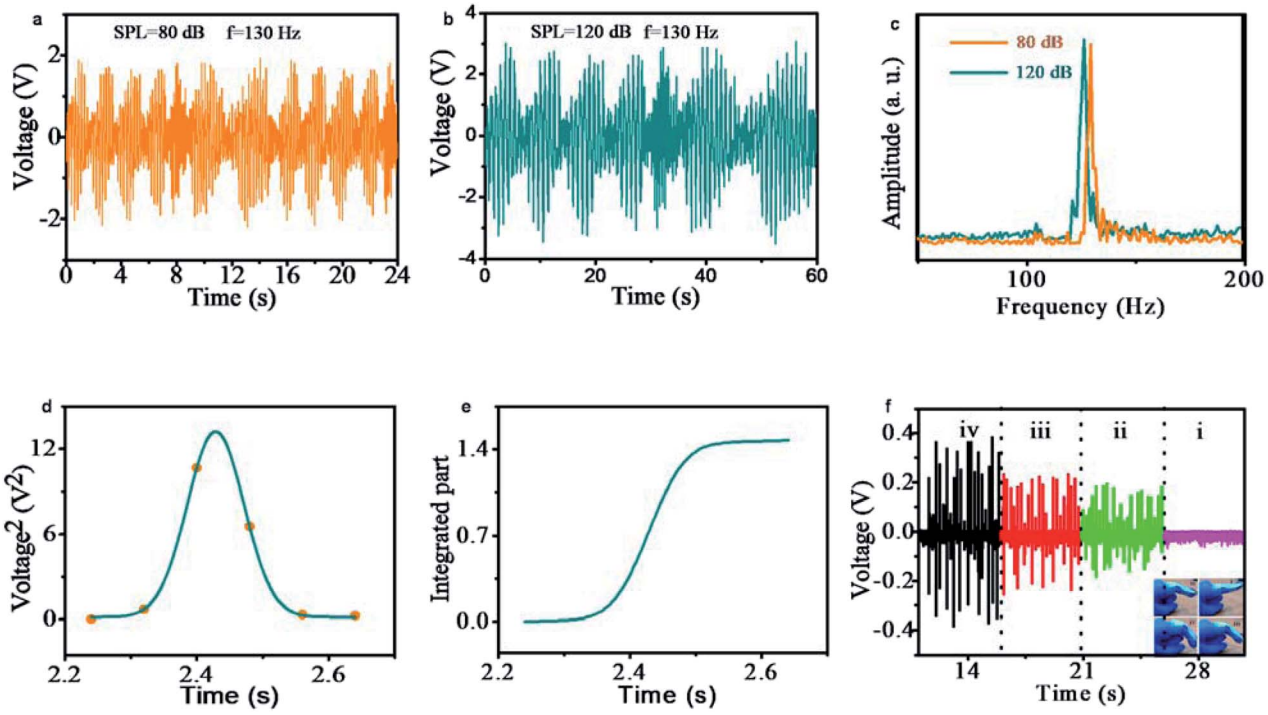

Fig. 3 Acoustoelectric energy harvester characterizations (a), (b) open circuit output voltage of the AAPNG under SPL 80 and 120 dB, respectively. (c) FFT processed frequency spectrum of the voltage signal in panels a and b. (d) The square of the output voltage (in panel b) for the integration to obtain the instantaneous electric power output. (e) The integration part of the time dependent V_{oc}. (f) The AAPNG output response in human finger bending-releasing movement oscillations; the right lower inset shows the digital photographs of AAPNG attached with a finger in bended movements.

$$P_a = \frac{Ap^2}{\rho c} \cos \varnothing, \quad (13)$$

where A is the area of the surface of the device, p is the sound pressure at 120 dB (20 Pa), ρ is the air density of 1.292 kg m^{-3}, c is the sound speed in air of 343.2 m s^{-1}, and $\varnothing$ is the angle between the direction of the sound propagation and the normal to the surface (zero degree in this case). Finally, the calculated acoustic power is $P_a \sim 0.000649$ W. Hence, the overall acoustoelectric energy conversion efficiency of AAPNG was found to be $\eta_{acoust} = \frac{P_e}{P_a} \times 100\% \approx 1.3\%$, which is superior to that of previous reports.[39] This extraordinary performance was compared over the previously developed devices in terms of the device materials, electrode materials and percentage of acoustoelectric energy conversion efficiency (% η_{acoust}), and is shown in Table S4, ESI.†

The piezoelectric and mechanical properties indicate that the Mg-salt filler added PVDF nanofiber can be a promising material for wearable energy generators. We showed the energy scavenging of AAPNG, which converts human movements into electrical energy. The applicability of AAPNG is in human finger monitoring as a finger sensor. In this case, the device was attached onto a human finger to measure the bending motions of the finger, as shown in the inset of Fig. 3f. Different angles of the finger bending-releasing motion oscillations corresponded to the variation of the output response (in terms of the voltage shown in Fig. 3f), which can help detect the finger motion states. To confirm the variation of the output bending-releasing responses in accordance with the finger movements, we demonstrate the different angle finger movements and recorded the different amplitude output response. At the starting point, the finger bending-releasing motion remains still, and no signal was generated, as indicated in Fig. 3f(i). Thereafter, the angle of the finger bending-releasing movement oscillations increased accordingly, and the output response increased, as indicated in Fig. 3f(ii)–(iv). When the finger was bending with a small angle amplitude ($0 < \theta < 30^\circ$) (as shown in the inset of Fig. 3f), the deformation device would respond, as depicted in Fig. 3f(ii). Once the finger bending angle amplitude was increased ($30^\circ < \theta < 60^\circ$) (see inset of Fig. 3f), the output response was increased like the output peak of Fig. 3f(iii). Again, the finger moving angle amplitude was larger ($60^\circ < \theta < 90^\circ$) (see inset of Fig. 3f), and comparatively high output response was detected, as shown in Fig. 3f(iv). This happened because as the bending angle became larger, the employed bending pressure amplitude on the nanofibers became higher, and the output voltage response improved significantly.[40] As a result of that, AAPNG is applicable as a strain sensor for measuring finger movement, and has effective usefulness in the rehabilitation training of patients.

As a potential application of energy harvesting technology, we demonstrated the powering of different types of commercial electrical units solely with the electricity generated from AAPNG attached to a speaker under music. The applicability of AAPNG was demonstrated through an amplifier circuit, the output of the amplifier was connected with a commercial capacitor, and it was charged up. Therefore, it can successfully and instantly power up the different types of commercial electrical units, such as red LED and LCD (shown in inset of Fig. 4b). Also, for the acoustic energy harvesting, the AAPNG was attached by

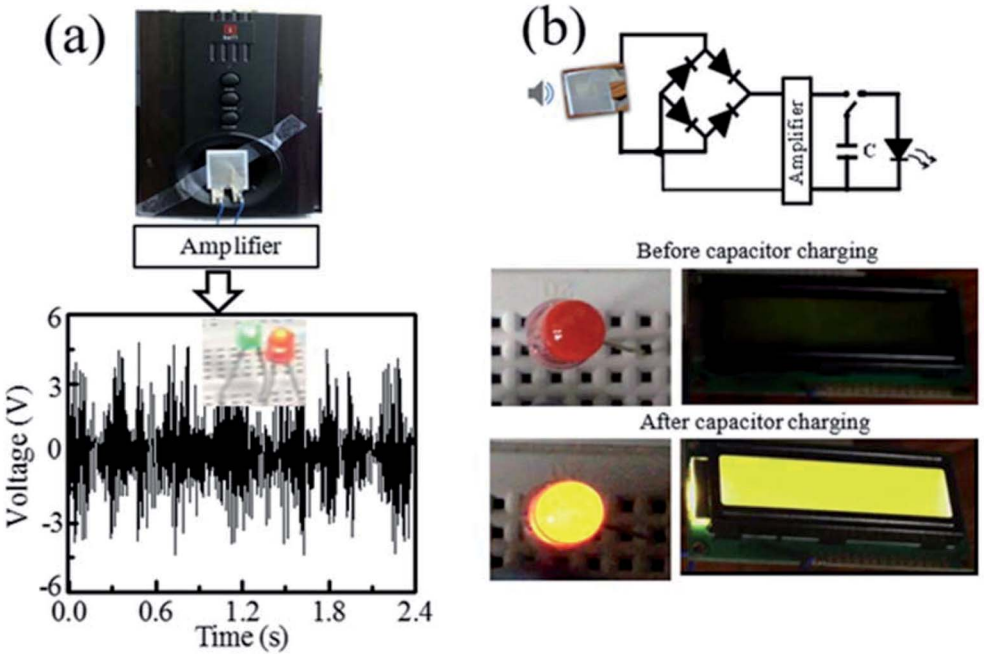

Fig. 4 (a) Set up for measurement, and the periodic output spike from the AAPNG driven by sound vibration from speaker (inset LEDs are ON when music bit is ON). (b) Schematic diagram of the operation mechanism of the capacitor storage performance driven by AAPNG, and it is able to turn on the red LED and liquid crystal display (LCD) instantly.

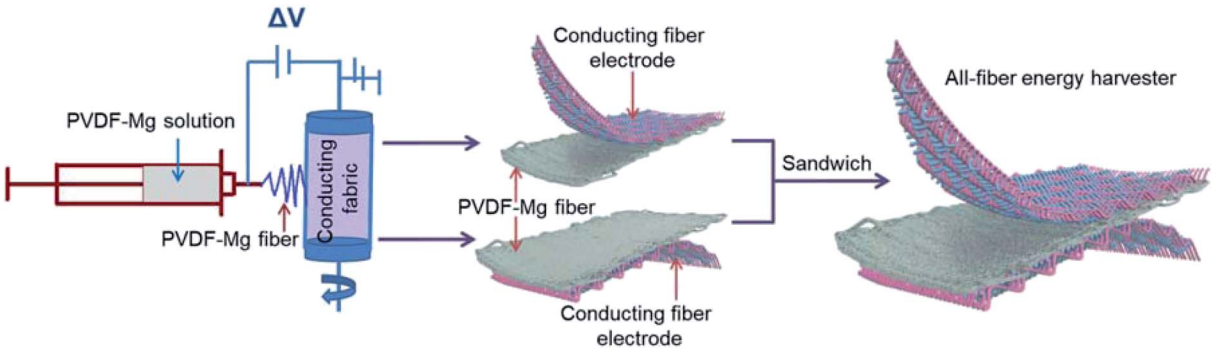

Fig. 5 Schematic of the fabrication procedure of AAPNG. It shows the PVDF–Mg fiber as an active piezoelectric material, and the microfiber-based conducting fabrics are the electrode.

a speaker and connected with amplifier the output voltage reached in ~7 V (shown in inset of Fig. 4a). It is clearly observed that the measured amplifier output voltage from the music also generated sufficient power to turn the LED on and off, as per music bit ON and OFF, respectively, providing a self-powered acoustic energy harvester.

3. Conclusions

In summary, we have demonstrated a Mg-salt added PVDF electrospun nanofiber-based all fiber acousto- and piezo-electric nanogenerator (AAPNG) for piezoelectric, as well as acoustic energy harvester, along with an ultrafast response in different sensory applications. The electrospinning process enables the simple, low cost, and large-scale production of composite fiber. The electroactive phase content ($F_{EA} \sim 87\%$), the overall crystallinity ($\chi_{ct} \sim 72\%$) and the β- and γ-phase content ($\chi_{c\beta} \sim 51\%$ and $\chi_{c\gamma} \sim 21\%$) in the PVDF–Mg nanofibers are superior to that of the neat PVDF nanofibers ($F_{EA} \sim 46\%$, $\chi_{ct} \sim 67\%$, $\chi_{c\beta} \sim 46\%$ and $\chi_{c\gamma} \sim 19\%$). As a result, the piezoelectric charge coefficient ($d_{33} \approx 33.6$ pC N^{-1}) and figure of merit (FoM $\approx 12.7 \times 10^{-12}$ Pa^{-1}) of the PVDF–Mg nanofibers are remarkably improved in comparison to those of the neat PVDF nanofibers. It is noteworthy to mention that AAPNG shows an excellent ultra-fast response time of ~6 ms, which makes the device more useful in the fast response sensory application for healthcare monitoring. The AAPNG generates a high electrical throughput (output voltage ~ 8.5 V and maximum power density ~0.28 μW cm^{-2} at a load resistance of 23 MΩ) under repeated finger imparting. Besides these properties, the developed device is useful as an acoustoelectric energy harvester, which generates an open circuit output voltage of 2 and 3 V at SPL of 80 and 120 dB, respectively, with a superior acoustoelectric sensitivity of ($S_a \sim 10$ V Pa^{-1}) and acoustoelectric conversion efficiency of ~1.3% in comparison to the neat PVDF nanofiber-based device. Since AAPNG shows higher sensitivity to the SPL at 80 dB, it is essentially useful for the detection of noise. The application of AAPNG is not limited to use in energy harvesting, but it is also useful for self-powering in the microphone for sound recording and human–machine interactions in future technology. Besides this, the maximum output voltage of 400 mV was obtained from the AAPNG when it was bending by the finger movement oscillations. Moreover, the application of AAPNG as a self-powered energy harvester is demonstrated by successfully powering up the commercial LED and LCD instantly when the capacitor is charged with the speaker sound vibration under SPL of 120 dB.

4. Experimental sections

Materials

Poly(vinylidene fluoride) (PVDF) pellets ($\bar{M}_w \sim 275\,000$, Sigma-Aldrich, USA). Magnesium chloride hexahydrate ($MgCl_2 \cdot 6H_2O$), *N*,*N*-dimethyl formamide (DMF, 99.5% of purity) and acetone (Merck Chemical, India). Ni–Cu plated polyester fabric (DE2-280C, EMS Inc., Korea). All materials were used without any further purification.

Fabrication of electrospun nanofibers

The PVDF solution (12 wt%) was processed by dissolving PVDF pellets in a mixture of DMF and acetone (mass ratio of 6 : 4) at 60 °C. Afterwards, the 1 wt% of Mg-salt was added to the PVDF/DMF and acetone solution. It was kept under magnetic stirring until the Mg-salts were uniformly dispersed in the PVDF solution and continuing for two days at room temperature. The final solution was then kept in a plastic syringe (10 mL) fitted with a stainless steel needle of tip-dimensions of 1.20 × 38 mm for electrospinning. The schematic of the electrospinning setup is shown in Fig. 5. The electrospinning process was carried out with a high-voltage power supply of 12 kV, and the distance between the needle and roller collector was 13 cm. The syringe pump was used to feed the polymer solution into the needle tip at a rate of 0.8 mL h^{-1}, and the electrospun fibers were collected in a grounded rotating collector. Finally, the electrospun fiber mat was dried at 60 °C for 12 h to eliminate the remaining solvents for further characterization and device fabrication.

Fabrication of AAPNG

We fabricated a simple low cost, lightweight and large rectangular area (~36 × 20 mm^2) of AAPNG, using the Mg-salt filler added PVDF electrospun fibers. The Ni–Cu plated polyester

conducting fabric electrode was used to collect the fiber during electrospinning. Then, the two nanofiber embedded fabric electrode was sandwiched by facing the nanofibers to each other, as shown in Fig. 5. The piezoelectric electrospun energy harvester (AAPNG) was prepared by simple Ni–Cu plated polyester conducting fabric as the top and bottom electrodes on both sides of the fiber mat (thickness $\sim$ 3.4 μm), and the total thickness of the device was 1503.4 μm. The schematic of the device fabrication is presented in Fig. 5.

5. Characterization

The crystalline phases of the Mg1.0 electrospun fibers were analyzed by Fourier Transform Infrared Spectroscopy (FT-IR) (Bruker, Tensor II). To study the degree of crystallinity of the electrospun fibers, X-ray diffraction (XRD) analysis was performed with a Bruker, D8 Advance, X-ray diffractometer, operated at 40 kV and 30 mA of current with Cu-K_α monochromatic radiation ($\lambda \sim 1.5406$ Å). The surface morphology of the electrospun fibers was carried out with a field emission scanning electron microscope (FE-SEM, FEI, INSPECT F50) run at an acceleration voltage of 20 kV. The piezoelectric and acoustic open circuit output voltage responses from AAPNG were recorded by means of a digital storage oscilloscope (Agilent, DSO3102A). The measured conductivity of the conducting fabric was 17 800 S m^{-1}, which indicates the highly conducting feature. Additionally, the measured current (I)–voltage (V) curve was linear (in between $\pm$0.2 V), which signifies the ohmic nature of the fabric. As a result, upon repetitive bending–unbending (releasing) cycles, a negligible change in the resistance was observed (ESI, Fig. S3†).

Conflicts of interest

The authors declare no competing financial interest.

Acknowledgements

This work was financially supported by a grant from the Science and Engineering Research Board (EEQ/2018/001130), Government of India. Krittish Roy is supported by DST-INSPIRE fellowship IF160559.

References

1 Z. L. Wang, *Adv. Mater.*, 2012, **24**, 280–285.
2 J. A. Paradiso and T. Starner, *Pervasive Comput.*, 2005, **4**, 18.
3 V. Bhatnagar and P. Owende, *Energy Sci. Eng.*, 2015, **3**, 153–173.
4 H. Chen, C. Xing, Y. Li, J. Wang and Y. Xu, *Sustain. Energy Fuels*, 2020, **4**, 1063–1077.
5 C. Garcia, I. Trendafilova, R. G. de Villoria and J. S. del Rio, *Nano Energy*, 2018, **50**, 401–409.
6 C. Garcia and I. Trendafilova, *Sens. Actuators, A*, 2019, **291**, 196–203.
7 C. Garcia, I. Trendafilova and J. S. del Rio, *Nano Energy*, 2019, **56**, 443–453.
8 Z. L. Wang, G. Zhu, Y. Yang, S. Wang and C. Pan, *Mater. Today*, 2012, **15**, 532–543.
9 D. Olmos, G. González-Gaitano, R. Vela, L. Córdoba, J. González-Benito and A. L. Kholkin, *Proceedings of ISAF-ECAPD-PFM*, 2012, Aveiro, pp. 1–3, DOI: 10.1109/ISAF.2012.6297828.
10 S. K. Ghosh, T. K. Sinha, B. Mahanty, S. Jana and D. Mandal, *J. Appl. Phys.*, 2016, **120**, 174501–174511.
11 Z. L. Wang and J. Song, *Science*, 2006, **312**, 242–246.
12 S. K. Ghosh, M. M. Alam and D. Mandal, *RSC Adv.*, 2014, **4**, 41886–41894.
13 S. K. Ghosh and D. Mandal, *Nano Energy*, 2018, **53**, 245–257.
14 B. Mahanty, S. K. Ghosh, S. Garain and D. Mandal, *Mater. Chem. Phys.*, 2017, **186**, 327–332.
15 X. Shi, W. Zhou, D. Ma, Q. Ma, D. Bridges, Y. Ma and A. Hu, *J. Nanomater.*, 2015, **2015**, 140716.
16 K. Park, S. Xu, Y. Liu, G. T. Hwang, S. J. L. Kang, Z. L. Wang and K. J. Lee, *Nano Lett.*, 2010, **10**, 4939–4943.
17 K. Maity, B. Mahanty, T. K. Sinha, S. Garain, A. Biswas, S. K. Ghosh, S. Manna, S. K. Ray and D. Mandal, *Energy Technol.*, 2017, **5**, 234–243.
18 S. Tiwari, A. Gaur, C. Kumar and P. Maiti, *Sustain. Energy Fuels*, 2020, **4**, 2469–2479.
19 A. Abutaleb, D. Lolla, A. Aljuhani, H. U. Shin, J. W. Rajala and G. G. Chase, *Fibers*, 2017, **5**, 33.
20 S. K. Ghosh, A. Biswas, S. Sen, C. Das, K. Henkel, D. Schmeisser and D. Mandal, *Nano Energy*, 2016, **30**, 621–629.
21 Y. J. Kim and C. R. Park, *Inorg. Chem.*, 2002, **41**, 6211–6216.
22 S. Garain, T. K. Sinha, P. Adhikary, K. Henkel, S. Sen, S. Ram, C. Sinha, D. Schmeiser and D. Mandal, *ACS Appl. Mater. Interfaces*, 2015, **7**, 1298–1307.
23 H. J. Sim, C. Choi, C. J. Lee, Y. T. Kim, G. M. Spinks, M. D. Lima, R. H. Baughman and S. J. Kim, *Adv. Eng. Mater.*, 2015, **17**, 1270–1276.
24 S. Jana, S. Garain, S. Sen and D. Mandal, *Phys. Chem. Chem. Phys.*, 2015, **17**, 17429–17436.
25 B. S. Ince-Gunduz, R. Alpern, D. Amare, J. Crawford, B. Dolan, S. Jones, R. Kobylarz, M. Reveley and P. Cebe, *Polymer*, 2010, **51**, 1485–1493.
26 G. Ico, A. Showalter, W. Bosze, S. C. Gott, B. S. Kim, M. P. Rao, N. V. Myung and J. Nam, *J. Mater. Chem. A*, 2016, **4**, 2293–2304.
27 D. Akinwande, N. Petrone and J. Hone, *Nat. Commun.*, 2014, **5**, 5678.
28 V. Bhavanasi, D. Y. Kusuma and P. S. Lee, *Adv. Energy Mater.*, 2014, **4**, 1400723.
29 L. Liang, X. Kang, Y. Sang and H. Liu, *Adv. Sci.*, 2016, **3**, 1500358.
30 C. Bao, Y. Guo, L. Song and Y. Hu, *J. Mater. Chem.*, 2011, **21**, 13942–13950.
31 H. Yu, T. Huang, M. Lu, M. Mao, Q. Zhang and H. Wang, *Nanotechnology*, 2013, **24**, 405401.
32 F. Guan, J. Wang, J. Pan, Q. Wang and L. Zhu, *Macromolecules*, 2010, **43**, 6739–6748.
33 D. Mandal, S. Yoon and K. J. Kim, *Macromol. Rapid Commun.*, 2011, **32**, 831–837.

34 H. J. Kim, J. H. Kim, K. W. Jun, J. H. Kim, W. C. Seung, O. H. Kwon, J. Y. Park, S. W. Kim and I. K. Oh, *Adv. Energy Mater.*, 2016, **6**, 15023–15029.
35 Z. Li, Q. Zheng, Z. L. Wang and Z. Li, *Research*, 2020, 8710686.
36 D. B. Deutz, J.-A. Pascoe, B. Schelen, S. Van Der Zwaag, D. M. De Leeuw and P. Groen, *Mater. Horiz.*, 2018, **5**, 444–453.
37 S. K. Ghosh and D. Mandal, *J. Mater. Chem. A*, 2020, DOI: 10.1039/D0TA08547B.
38 C. Lang, J. Fang, H. Shao, H. Wang, G. Yan, X. Ding and T. Lin, *Nano Energy*, 2017, **35**, 146–153.
39 C. C. Chen, W. Y. Yan, Y. Y. Wu and C. C. Ting, *Int. J. Eng. Techn. Inn.*, 2014, **4**, 86–95.
40 M. Zhang, T. Gao, J. Wang, J. Liao, Y. Qiu, H. Xue, Z. Shi, Z. Xiong and L. Chen, *Nano Energy*, 2015, **11**, 510–517.